J|A|C|S
ARTICLES
Published on Web 01/23/2007

X-ray Photoelectron Spectroscopy and First Principles Calculation of BCN Nanotubes

Shin Young Kim,[†] Jeunghee Park,*[,†] Hyun Chul Choi,[‡] Jae Pyung Ahn,[§] Jin Qiang Hou,[||,⊥] and Hong Seok Kang*[,||]

Contribution from the Department of Chemistry, Korea University, Jochiwon 339-700, Korea, Environment and Energy Division, Korea Institute of Industrial Technology, Chonan 330-825, Korea, Nano-Material Research Center, Korea Institute of Science and Technology, Seoul 136-791, Korea, and Department of Nano and Advanced Materials, College of Engineering, Jeonju University, Hyoja-dong, Wanda ku, Chonju, Chonbuk 560-709, Korea

Received October 24, 2006; E-mail: parkjh@korea.ac.kr; hsk@jj.ac.kr

Abstract: Multiwalled boron carbonitride (BCN) nanotubes with two different structures were synthesized via thermal chemical vapor deposition; one has 10% C atoms homogeneously doped into BN nanotubes ($B_{0.45}C_{0.1}N_{0.45}$ NTs), and the other has BN layers sheathed with 5-nm-thick C outerlayers (BN−C NTs). The electronic structures of the B, C, and N atoms were thoroughly probed by synchrotron X-ray photoelectron spectroscopy and the X-ray absorption near-edge structure method. The $B_{0.45}C_{0.1}N_{0.45}$ NTs contain a significant amount of B−C and C−N bonding with a pyridine-like structure (hole structure), which reduces the π bonding states of the B and N atoms. From the XPS valence band spectrum, the band gap was estimated to be about 2.8 eV. In the BN−C NTs, the C and BN domains are separated without forming the pyridine-like structure. Using the first principles method, we investigated the relative stabilities and electronic structures of the various isomers of the double-walled (12,0)@(20,0) BCN NTs. The C-outerlayer BN nanotube structure is the most stable isomer, when there exist no defects in the tubes with B/N = 1.0 (i.e., *graphite-like structure*). In addition, a reasonable model, which is characterized by the motives consisted of three *pyridine-like* rings around a hollow site, is presented for the local structure of C atoms in the $B_{0.45}N_{0.45}C_{0.1}$ NTs. A considerable decrease of the band gap due to the 10% C doping was predicted, which was consistent with the experimental results.

1. Introduction

Since the discovery of carbon nanotubes (CNTs) in 1991,[1] extensive research has been conducted to find novel tubular structures, among which ternary boron carbonitride nanotubes (BCN NTs) have attracted increasing interest because of their unique electronic properties and potential nanotechnological applications. A prime advantage of these BCN NTs over their carbon counterparts is the relative simplicity with which their electronic properties can be controlled. Theoretical calculations have revealed that the band structure of BCN NTs can be tuned simply by changing their atomic compositions and configurations.[2−6] For example, Liu et al. proposed three possible atomic arrangements for BC_2N film and concluded that two of them would be semiconductors (the lowest band gap is 1.6 eV), and the other, metallic.[3] The band gap of BC_2N films was also measured to be either 2.1 or 1.4 eV, depending on the measurement method.[7] In fact, the synthesis and characterization of bulk BCN compounds have been an important issue, because of their wide range of prospective applications as superhard protective materials.[8,9] The calculation predicted a high Young's modulus for the single-walled BC_3 and BC_2N NTs, comparable to that of CNTs.[10] Therefore, BCN NTs are particularly useful for nanodevice applications where high-strength and semiconductor properties are desired.

In terms of their structural stability, theoretical calculations predict that segregation of the BN, C, and BCN domains tends to occur; the most stable structure seems to optimize the chemical bond energy by maximizing the number of C−C and B−N bonds.[3−5] There has been much effort to synthesize BCN NTs using various methods, e.g., the arc discharge, hot-filament

[†] Korea University.
[‡] Korea Institute of Industrial Technology.
[§] Korea Institute of Science and Technology.
[||] Jeonju University.
[⊥] Permanent address: Pohl Institute of Solid-state Physics, Tongji University, Shanghai 200092, P. R. China.

(1) Iijima, S. *Nature* **1991**, *56*, 354.
(2) Miyamoto, Y.; Rubio, A.; Cohen, M. L.; Louie, S. G. *Phys. Rev. B* **1994**, *50*, 4976.
(3) Liu, A. Y.; Wentzcovitch, R. M.; Cohen, M. L. *Phys. Rev. B* **1989**, *39*, 1760.
(4) (a) Blase, X.; Charlier, J.-Ch.; De Vita, A.; Car, R. *Appl. Phys. Lett.* **1997**, *70*, 197. (b) Blase, X.; Charlier, J.-Ch.; De Vita, A.; Car, R. *Appl. Phys. A* **1999**, *68*, 293.
(5) Nozaki, H.; Itoh, S. *J. Phys. Chem. Solids* **1996**, *57*, 41.
(6) Enyashin, A. N.; Makurin, Yu. N.; Ivanovskii, A. L. *Carbon* **2004**, *42*, 2081.
(7) (a) Watanabe, M. O.; Itoh, S.; Sasaki, T.; Mizushima, K. *Phys. Rev. Lett.* **1996**, *77*, 187. (b) Chen, Y.; Barnard, J. C.; Palmer, R. E.; Watanabe, M. O.; Sasaki, T. *Phys. Rev. Lett.* **1999**, *83*, 2406.
(8) Kawaguchi, M. *Adv. Mater.* **1997**, *9*, 615.
(9) Solozhenko, V. L.; Andrault, D.; Fiquet, G.; Mezouar, M.; Rubie, D. C. *Appl. Phys. Lett.* **2001**, *78*, 1385.
(10) Hernández, E.; Goze, C.; Bernier, P.; Rubio, A. *Phys. Rev. Lett.* **1998**, *80*, 4502.

10.1021/ja067592r CCC: $37.00

assisted, or thermal chemical vapor deposition (CVD) methods.[11−18] So far, nanotubes with a homogeneous BCN composition or separated phases of BN and C layers have been observed. Their structure and composition appear to be sensitive to the growth method and actual growth parameters. Therefore, systematic studies of the characteristics of BCN NTs grown using specific techniques are of great importance both to further their utilization and to develop suitable fabrication methods. To do so, it is clear that elucidation of their electronic states is indispensable to characterize the BCN NTs. However, the electronic states of the BCN NTs, especially the state-resolved distributions of their compositional elements, are far from being well scrutinized.

In the present work, we prepared two different types of multiwalled BCN NTs by the thermal CVD method; one type has 10% C doped into the BN NTs ($B_{0.45}C_{0.1}C_{0.45}$), and the other has BN layers sheathed with 5-nm-thick C outerlayers (BN−C). Detailed analytical investigations of the electronic structures of the BCN NTs were performed systematically using synchrotron X-ray photoelectron spectroscopy (XPS) and the X-ray absorption near-edge structure (XANES) method. Since the escape depth of a photoelectron increases with its kinetic energy, a higher photon energy provides more information on the inner parts of the nanostructures.[19] In the present work, the XPS photon energy was varied in the range of 360−1265 eV. The XPS valence band spectrum, photoluminescence (PL), and cathodoluminescence (CL) of the BCN NTs were investigated in order to determine their band gap. The morphology and structure of these two nanostructures were analyzed by means of scanning electron microscopy (SEM), transmission electron microscopy (TEM), electron energy-loss spectroscopy (EELS), and Raman spectroscopy.

Moreover, in order to gain further insight into the electronic structures of the synthesized BCN NTs, we investigated various isomers of the double-walled (12,0)@(20,0) BCN NTs using the first principles method. The results suggest that the relative stabilities of the isomers are sensitive to the presence of hollow pyridine-like defects and the arrangement of the C atoms and that the difference in the electronic structures originates mainly from the formation of a pyridine-like structure. To the best of our knowledge, this is the first time that the electronic structures of BCN NTs have been investigated by both experimental and theoretical methods.

2. Experimental Section

B pieces (99%, MaTeck) and BN powders (99%, Aldrich) were ball-milled separately for 20 h, using a mechanical ball mill system (Spex 8000M). These ball-milled powders and iron phthalocyanine ($FeC_{32}N_8H_{16}$, hereafter designated as FePc) were placed in an alumina boat inside a quartz tube reactor. Alumina substrates were coated with $FeCl_2 \cdot 4H_2O$ (99%, Aldrich) ethanol solution, producing Fe nanoparticles deposited on the substrates. These substrates were used to cover the boat containing the source. NH_3 gas was introduced into the quartz tube when the temperature reached 1200 °C. The amount of FePc was varied to control the C content of the products. After 2 h of growth, a white colored product with a gray tint deposited homogeneously over a large area of the substrates. The size, structure, and composition of the product were examined by SEM (Hitachi S-4300), field-emission TEM (FEI TECNAI G^2 200 kV and Jeol JEM 2100F), EELS (GATAN GIF-2000) attached to TEM (TECNAI G^2), and Raman spectroscopy (Renishaw 1000) using the 514.5 nm line of an argon ion laser. Room-temperature CL (Gatan MonoCL2) measurement was performed at an acceleration voltage of 10 kV. Temperature-dependent PL measurements were carried out using a cw He−Cd laser ($\lambda = 325$ nm) as the excitation source.

The XPS measurements were performed at the U7 beam line of the Pohang Light Source (PLS). The detailed experimental conditions are described elsewhere.[19] Briefly, the XPS data were collected using photon energies in the range 360−1265 eV, with a photon flux within the range $7 \times 10^{11}-3 \times 10^{10}$ (photons/s/200mA). The binding energies were corrected for specimen charging by referencing the C 1s peak to 284.6 eV. The experiment was performed in an ultrahigh vacuum (UHV) chamber with a base pressure $\leq 5 \times 10^{-10}$ Torr. The energy of the photoelectrons emitted from the surface of the nanotubes was analyzed with an electron energy analyzer (Physical Electronics: model PHI 3057 with a 16-channel detector). The analyzer was located at an angle of 55° from the surface normal. The B and N K-edges XANES measurement was also performed at the same beam line. The spectral resolving power ($E/\Delta E$) of the incident photons is about 5000 at 400 eV. The angle of the incident X-ray beam to the sample plane was tuned from 15° to 90°. All of the spectra were taken in total electron yield mode in which the sample current was recorded at room temperature.

Total energy calculations were carried using the Vienna ab initio simulation package (VASP).[20] The electron-ion interactions were described by the projected augmented wave (PAW) method,[21] which

(11) Redlich, Ph.; Loeffler, J.; Ajayan, P. M.; Bill, J.; Aldinger, F.; Rühle, M. *Chem. Phys. Lett.* **1996**, *260*, 465.
(12) (a) Suenaga, K.; Colliex, C.; Demoncy, N.; Loiseau, A.; Pascard, H.; Willaime, F. *Science* **1997**, *278*, 653. (b) Zhang, Y.; Gu, H.; Suegana, K.; Iijima, S. *Chem. Phys. Lett.* **1997**, *279*, 264.
(13) Sen, R.; Satishkumar, B. C.; Govindaraj, A.; Harikumar, K. R.; Raina, G.; Zhang, J.-P. Cheetham, A. K.; Rao, C. N. R. *Chem. Phys. Lett.* **1998**, *287*, 671.
(14) (a) Terrones, M.; Benito, A. M.; Manteca-Diego, C.; Hsu, W. K.; Osman, O. I.; Hare, J. P.; Reid, D. G.; Terrones, H.; Cheetham, A. K.; Prassides, K.; Kroto, H. W.; Walton, D. R. M. *Chem. Phys. Lett.* **1996**, *257*, 576. (b) Terrones, M.; Grobert, N.; Terrones, H. *Carbon* **2002**, *40*, 1665. (c) Terrones, M.; Golberg, D.; Grobert, N.; Seeger, T.; Reyes-Reyes, M.; Mayne, M.; Kamalakaran, R.; Dorozhkin, P.; Dong, Z.-C.; Terrones, H.; Rühle, M.; Bando. Y. *Adv. Mater* **2003**, *15*, 1899.
(15) (a) Han, W.; Bando, Y.; Kurashima, K.; Sato, T. *Appl. Phys. Lett.* **1998**, *73*, 3085. (b) Golberg, D.; Bando, Y.; Kurashima, K.; Sato, T. *Chem. Phys. Lett.* **2000**, *323*, 185. (c) Golberg, D.; Dorozhkin, P.; Bando, Y.; Hasegawa, M.; Dong, Z.-C. *Chem. Phys. Lett.* **2002**, *359*, 220. (d) Golberg, D.; Bando, Y.; Mitome, M.; Kurashima, K.; Grobert, N.; Reyes-Reyes, M.; Terrones, H.; Terrones, M. *Chem. Phys. Lett.* **2002**, *360*, 1. (e) Golberg, D.; Bando, Y.; Mitome, M.; Kurashimaa, K.; Satoa, T.; Grobert, N.; Reyes-Reyes, M.; Terrones, H.; Terrones, M. *Physica B* **2002**, *323*, 60. (f) Golberg, D.; Dorozhkin, P. S.; Bando, Y.; Dong, Z.-C.; Grobert, N.; Reyes-Reyes, M.; Terrones, H.; Terrones, M. *Appl. Phys. Lett.* **2003**, *82*, 1275. (g) Vinu, A.; Terrones, M.; Golberg, D.; Hishita, S.; Ariga, K.; Mori, T. *Chem. Mater.* **2005**, *17*, 5887. (h) Yin, L.-W.; Bando, Y.; Golberg, D.; Gloter, A.; Li, M.-S.; Yuan, X.; Sekiguchi, T. *J. Am. Chem. Soc.* **2005**, *127*, 16354. (i) Golberg, D.; Dorozhkin, P. S.; Bando, Y.; Mitome, M.; Tang, C. C. *Diamond Relat. Mater.* **2005**, *14*, 1857.
(16) (a) Bai, X. D.; Yu, J.; Liu, S.; Wang, E. G. *Chem. Phys. Lett.* **2000**, *325*, 485. (b) Yu, J.; Bai, X. D.; Ahn, J.; Yoon, S. F.; Wang, E. G. *Chem. Phys. Lett.* **2000**, *323*, 529. (c) Bai, X. D.; Guo, J. D.; Yu, J.; Wang, E. G.; Yuan, J.; Zhou, W. *Appl. Phys. Lett.* **2000**, *76*, 2624. (d) Bai, X. D.; Wang, E. G.; Yu, J.; Yang, H. *Appl. Phys. Lett.* **2000**, *77*, 67. (e) Yu, J.; Ahn, J.; Yoon, S. F.; Zhang, Q.; Rusil, B.; Gan, B.; Chew, K.; Yu, M. B.; Bai, X. D.; Wang, E. G. *Appl. Phys. Lett.* **2000**, *77*, 1949. (f) Guo, J. D.; Zhi, C. Y.; Bai, X. D.; Wang, E. G. *Appl. Phys. Lett.* **2002**, *80*, 124. (g) Zhi, C. Y.; Guo, J. D.; Bai, X. D.; Wang, E. G. *J. Appl. Phys.* **2002**, *91*, 5325. (h) Zhi, C. Y.; Bai, X. D.; Wang, E. G. *Appl. Phys. Lett.* **2002**, *80*, 3590. (i) Wang, W. L.; Bai, X. D.; Liu, K. H.; Xu, Z.; Golberg, D.; Bando, Y.; Wang, E. G. *J. Am. Chem. Soc.* **2006**, *128*, 6530.
(17) (a) Weng-Sieh, Z.; Cherrey, K.; Chopra, N. G.; Blase, X.; Miyamoto, Y.; Rubio, A.; Cohen, M. L.; Louie, S. G.; Zettl, A.; Gronsky, R. *Phys. Rev. B* **1995**, *51*, 11229. (b) Han, W.-Q.; Cumings, J.; Zettl, A. *Appl. Phys. Lett.* **2001**, *78*, 2769. (c) Han, W.-Q.; Comings, J.; Huang, X.; Bradley, K.; Zettl, A. *Chem. Phys. Lett.* **2001**, *346*, 368. (d) Han, W.; Mickelson, W.; Cumings, J.; Zettl, A. *Appl. Phys. Lett.* **2002**, *81*, 1110. (e) Wu, J.; Han, W.-Q.; Walukiewicz, W.; Ager, J.-W., III; Shan, W.; Haller, E. E.; Zettl, A. *Nano Lett.* **2004**, *4*, 647. (f) Chang, C. W.; Han, W.-Q.; Zettl, A. *Appl. Phys. Lett.* **2005**, *86*, 173102.
(18) Wang, R. M.; Zhang, H. Z. *New J. Phys.* **2004**, *6*, 78.
(19) (a) Choi, H. C.; Park, J. *J. Phys. Chem. B* **2005**, *109*, 4333. (b) Choi, H. C.; Bae, S. Y.; Jang, W. S.; Kim, S. Y.; Park, J.; Song, H. J.; Shin, H.-J.; Jung, H.; Ahn, J.-P. *J. Phys. Chem. B* **2005**, *109*, 1683.
(20) (a) Kresse, G.; Hafner, J. *Phys. Rev. B* **1993**, *47*, RC558. (b) Kresse, G.; Furthmuller, J. *Phys. Rev. B* **1996**, *54*, 11169.

is basically a frozen-core all-electron calculation. The exchange-correlation effect was treated within the local density approximation (LDA). The solution of the Kohn−Sham (KS) equation was obtained using the Davison blocked iteration scheme, followed by the residual vector minimization method. All valence electrons of chemical elements are explicitly considered in the KS equation. We adopt a supercell geometry in which *k*-space sampling is done with 2 or 4 *k*-points in the irreducible region of the first Brillouin zone along the tube axis, depending upon the size of the supercell. In doing this, we use large supercells which guarantee the interatomic distances between neighboring cells greater than 7.00 Å. The cutoff energy is set high (=400 eV) enough to ensure accurate results, and the conjugate gradient method is employed to optimize the geometry until the Hellmann−Feynman force exerted on an atom is less than 0.03 eV/Å. The reliability of the PAW method was confirmed in our recent calculations of the electronic and chemical properties of various systems ranging from metal−aromatic sandwich complexes to nanotubes.[22]

3. Results

3.1. Morphology and Structure: SEM and TEM. We prepared three samples; (1) multiwalled BN NTs mixed with CNTs; (2) 10%-C doped BN NTs (hereafter designated as "$B_{0.45}C_{0.1}N_{0.45}$ NTs"), and (3) C-outerlayered BN NTs (hereafter designated as "BN−C NTs"), by adjusting the weight ratio of the B and C sources. When the weight ratio of the C/B source was 1:1, the products were BN−C NTs. With a higher weight ratio of the C source (C/B = 2:1), $B_{0.45}C_{0.1}N_{0.45}$ NTs were produced. BN NTs were grown together with CNTs when C/B = 1:2.

Figure 1a shows the SEM image for the high-density $B_{0.45}C_{0.1}N_{0.45}$ NTs grown on a large area of the substrates. Their length is in the range 20−30 μm. The surface is clean without any nanoparticles and periodically bumpy over the entire nanotubes. The TEM image shows a typical morphology consisting of a bamboolike structure in which the inside of the nanotubes is separated by a series of compartment layers [Figure 1b]. The diameter of the nanotubes is in the range 80−150 nm with an average value of 100 nm, and roundly curved compartment layers appear periodically with a distance of 150−300 nm between them (about 2 times the diameter). The high-resolution TEM (HRTEM) image shows that the nanotubes consisted of successive compartment layers [Figure 1c]. The atomic-resolved image for the edge of the wall part shows the (002) basal planes aligned along the tube axis, with a high degree of crystalline perfection [Figure 1d]. The spots in the fast Fourier-transformed ED (FFT ED) pattern can be indexed as the (002) basal planes of the *h*-BN layers [inset of Figure 1d]. Further analysis revealed that the BN−C NTs and BN NTs have the same bamboolike structures and crystalline perfection as those of the $B_{0.45}C_{0.1}N_{0.45}$ NTs.

3.2. EELS: Spatial Distribution of B, C, and N. Figure 2 shows the EELS spectrum for the edge and center parts along the cross section of the nanotubes. The spot size of the electron probe is about 5 nm. Figure 2a displays the EELS spectrum of the BN NTs whose energy-filtered TEM image is shown in the inset. The spectrum shows two distinct absorption features corresponding to the known K-shell ionization edges of the B and N atoms starting from 192 and 401 eV, respectively, revealing that the nanostructures are composed of sp^2 hybridized *h*-BN sheets. Figure 2b shows the EELS spectrum for the edge and center parts of the $B_{0.45}C_{0.1}N_{0.45}$ NTs. Its energy-filtered TEM image is shown in the inset. The spectrum shows three distinct absorption features corresponding to the K-shell ionization edges of the B, C, and N atoms. A detailed inspection of the near-edge fine structure of the C atoms shows a sharply defined π^* feature at 288 eV and a broad σ^* feature, corresponding to the sp^2 hybridization states. The near-edge fine structure of the B and N atoms also confirms their sp^2 hybridization state, which is distinguished by their sharply defined 1s → π^* and 1s → σ^* transition. For all parts, the average value of the C concentration, defined as the [C]/([B] + [C] + [N]) atomic ratio, was found to be uniformly about 0.1 (with 10% uncertainty), using software (DigitalMicrograph for GMS1.2, Gatan Inc.).

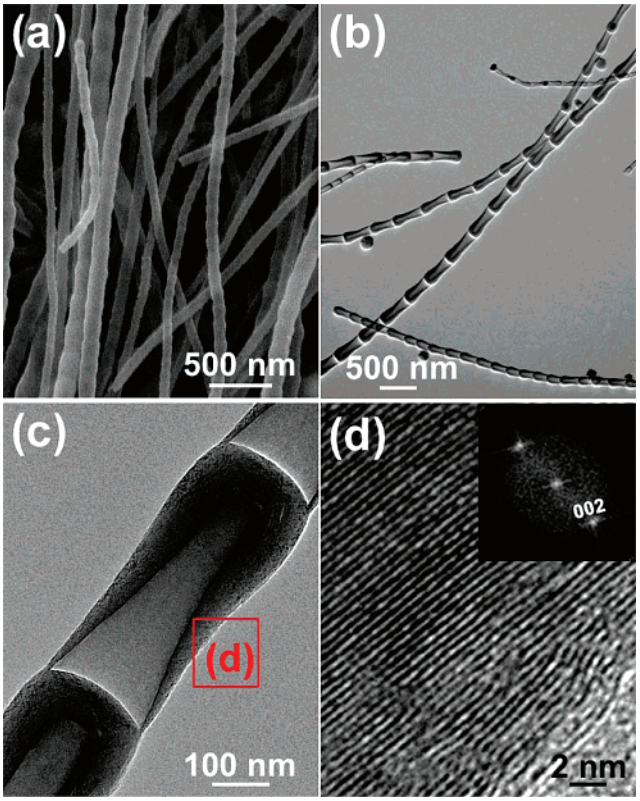

Figure 1. (a) SEM micrograph showing the high-density $B_{0.45}C_{0.1}N_{0.1}$ NTs grown on the substrates and their clean and periodically bumpy surface. (b) TEM image showing a bamboolike structure. (c) HRTEM image shows that the nanotubes consisted of successive compartment layers. (d) Atomic-resolved image for the edge part of the wall layers with its corresponding FFT ED pattern (inset).

Figure 2c shows the EELS spectrum for the edge and center parts of the BN−C NTs. The corresponding energy-filtered TEM image is shown in the inset. At the edges, the C K-edge feature is dominant over the B and N K-edge feature. The C composition at the edge parts reaches 0.75. However, at the center part, the C K-edge features are not detected. Figure 2d shows the elemental distribution of the B, C, and N atoms along the cross section of the BN−C NT, showing only the C component at the 5-nm-thick edge parts. Therefore, we conclude that the BN NTs are sheathed with C outerlayers.

(21) Kresse, G.; Joubert, D. *Phys. Rev. B* **1999**, *59*, 1758.
(22) (a) Kang, H. S. *J. Phys. Chem. A* **2005**, *109*, 478. (b) Kang, H. S. *J. Phys. Chem. A* **2005**, *109*, 1458. (c) Kang, H. S. *J. Phys. Chem. A* **2005**, *109*, 4342. (d) Kang, H. S. *J. Am. Chem. Soc.* **2005**, *127*, 9839. (e) Kang, H. S. *J. Phys. Chem. A* **2005**, *109*, 9292. (f) Kang, H. S. *J. Phys. Chem. B* **2006**, *110*, 4621. (g) Kang, H. S. *J. Phys. Chem. A* **2006**, *110*, 4780.

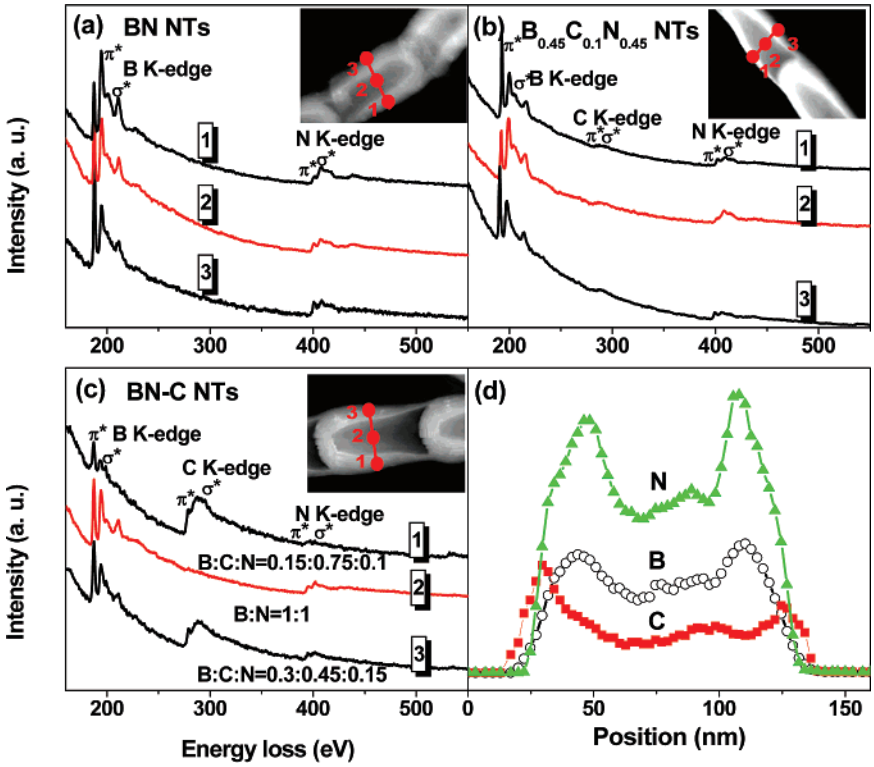

Figure 2. EELS for the edge (marked by "1" and "3") and the center (marked by "2") parts of the (a) BN NT, (b) $B_{0.45}C_{0.1}N_{0.45}$ NT, and (c) BN−C NT. The insets display the energy-filtered TEM images with the number representing the probing position of EELS. The spectrum shows three distinct absorption features starting at 192, 288, and 401 eV, corresponding to the known K-shell ionization edges of B, C, and N, respectively. (d) The elemental distribution of the B, C, and N atoms along the cross section of the BN−C NT, showing the C outerlayers (thickness = 5 nm) sheathing the BN NT.

3.3. Fine-Scanned XPS: Electronic Structure of B, C, and N Atoms. We measured the survey-scanned XPS of the BN NTs, $B_{0.45}C_{0.1}N_{0.45}$, and BN−C NTs using various photon energies in the range 350−1265 eV (Supporting Information, Figure S1). We also synthesized pure BN NTs (without any CNT impurities) but failed to measure their synchrotron XPS spectra, because their conductivity was too low to yield any current signal. As the photon energy increases, the average probing depth of the B, C, and N 1s electrons increases from 1 to 5 nm.[23] The relative ratio of the B, C, and N atoms was estimated from the area ratio of the B, C, and N 1s peaks and the sensitivity factors. The C content of the $B_{0.45}C_{0.1}N_{0.45}$ NTs remains constant at 0.15 ± 0.05, irrespective of the photon energy. This homogeneous C doping is consistent with the EELS data (within the experimental error). In contrast, the C content of the BN−C NTs decreases from 0.2 ± 0.1 to 0.1 ± 0.05 as the photon energy increases from 475 to 912 eV, which indicates the C outerlayers sheathing the BN NTs, as predicted from the EELS data.

In order to probe the electronic structures of the $B_{0.45}C_{0.1}N_{0.45}$ and BN−C NTs, we measure their fine-scanned B, C, and N 1s peaks (Figures 3 and 4). For comparison, the fine-scanned B and N 1s XPS of the BN NTs (mixed with CNTs) and *h*-BN powders are measured (Supporting Information, Figures S2−S3 and Tables S1−S2).

Figure 3a shows the B 1s spectrum of the $B_{0.45}C_{0.1}N_{0.45}$ NTs, measured using three photon energies (475, 635, and 1265 eV). The band is much broader in width and more asymmetric, as compared to that of the BN NTs. This band can thus be deconvoluted into three bands at 189.6 (PB0), 190.7 (PB1), and 192.5 (PB2) eV, respectively. The binding energy of the B atoms bonded to the C atoms would be expected to appear at a lower energy compared to that of the B atoms bonded to the N atoms, and at a higher energy relative to that of the B atoms bonded to dangling bonds or defects (usually bonded to more electronegative O atoms). Therefore the B0, B1, and B2 bands can be assigned to the B−C, B−N, and B−O bonding structures, respectively. This assignment is consistent with previous studies of BCN films, based on the electronegativity differences between the atoms, i.e., B < C < N < O.[24−28] The width and area % values of the three resolved bands are nearly independent of the photon energy, with the average area % values of the PB0, PB1, and PB2 bands being 36, 42, and 22, respectively (Table 1). This result indicates that the C doping occurs homogeneously over the cross section of the BN NTs.

Figure 3b displays the C 1s spectrum of the $B_{0.45}C_{0.1}N_{0.45}$ NTs, showing a broad band centered at 285 eV. This can be deconvoluted into three bands at 283.5 (PC0), 284.6 (PC1), and 286.3 (PC2) eV, respectively. The binding energy of the C atoms bonded to the B, C, and N atoms would be expected to follow the order C−B < C−C < C−N, as predicted from the electronegativity differences between the three atoms B < C < N. Therefore, the PC0, PC1, and PC2 bands can be assigned to

(23) Teo, B. K. *EXAFS: Basic Principles and Data Analysis*; Springer-Verlag: Berlin, 1986; p 92.

(24) Uddin, Md. N.; Shimoyama, I.; Yuji Baba, Y.; Sekiguchi, T.; Nagano, M. *J. Vac. Sci. Technol.* **2005**, *23*, 497.
(25) Linss, V.; Rodilb, S.; Reinkec, P.; Garnierd, M.; Oelhafend, P.; Kreissige, U.; Richtera, F. *Thin Solid Films* **2004**, *467*, 76.
(26) Bejarano, G.; Caicedo, J.; Baca, E.; Prieto, P.; Balogh, A.; Enders, S. *Thin Solid Films* **2006**, *494*, 53.
(27) Zhou, F.; Adachi, K.; Kato, K. *Thin Solid Films* **2006**, *497*, 210.
(28) Morant, C.; Prieto, P.; Bareno, J.; Sanz, J. M.; Elizalde, E. *Thin Solid Films* **2005**, *515*, 207.

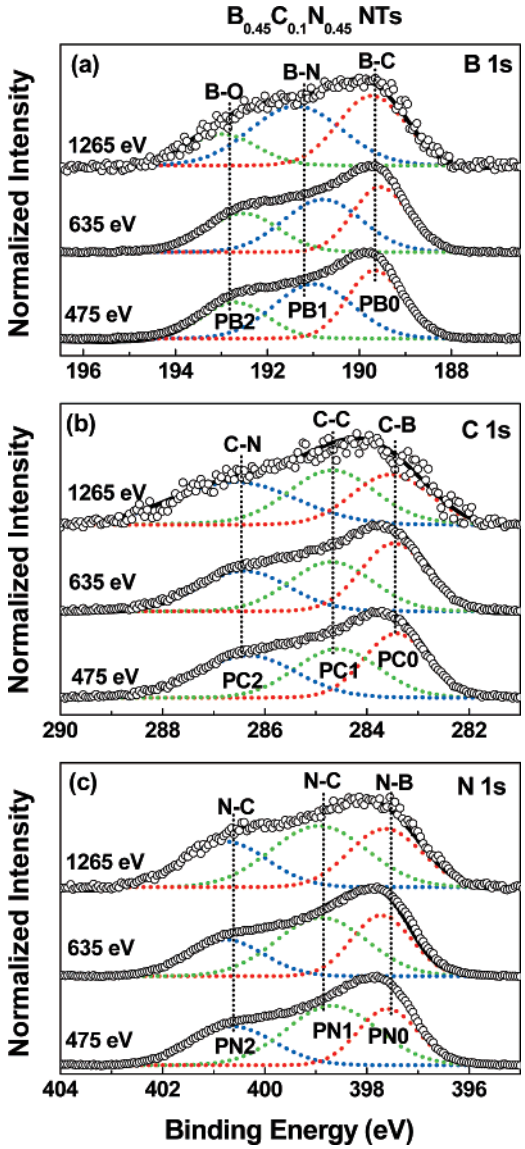

Figure 3. (a) The B 1s XPS spectrum of the $B_{0.45}C_{0.1}N_{0.45}$ NTs, using 360, 625, and 1265 eV. The data points (○) of the B 1s band are fitted by three Voigt functions, PB0, PB1, and PB2 (dotted lines). (b) The C 1s XPS spectrum of the BN NTs. The data points (○) of the N 1s band are fitted by three Voigt functions, PC0, PC1, and PC2 (dotted lines). (c) The N 1s XPS spectrum of the BN NTs. The data points (○) of the N 1s band are fitted by three Voigt functions, PN0, PN1, and PN2 (dotted lines).

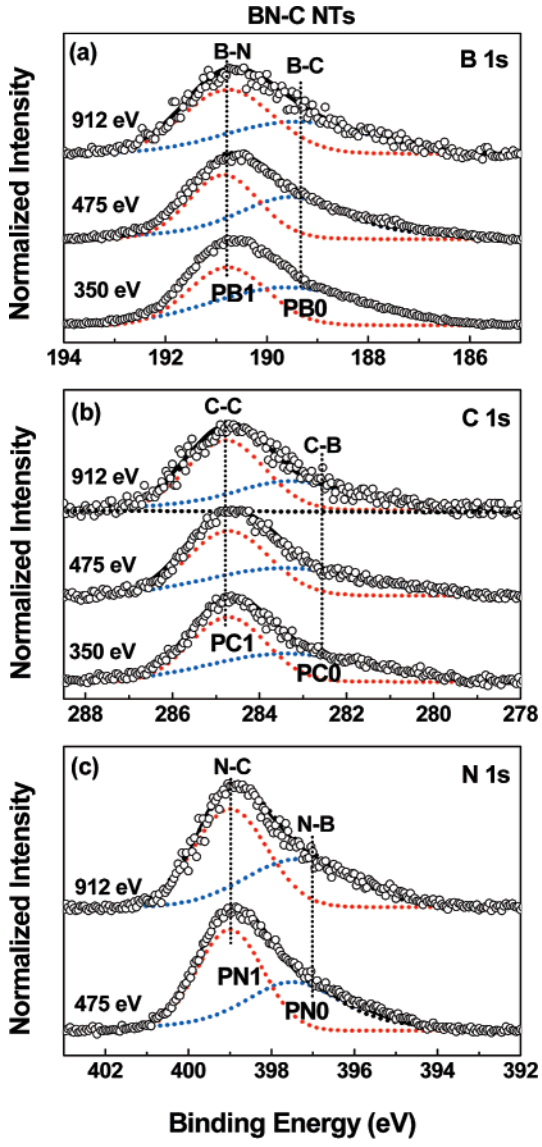

Figure 4. (a) The B 1s XPS spectrum of the BN−C NTs, using 350, 475, and 912 eV. The data points (○) of the B 1s band are fitted by two Voigt functions, PB0 and PB1 (dotted lines). (b) The C 1s XPS spectrum of the BN−C NTs. The data points (○) of the N 1s band are fitted by two Voigt functions, PC0 and PC1 (dotted lines). (c) The N 1s XPS spectrum of the BN−C NTs. The data points (○) of the N 1s band are fitted by two Voigt functions, PN0 and PN1 (dotted lines).

the C−B, C−C, and C−N bonding structures, respectively. The highest energy PC2 band would include the other binding configurations, such as C═O or C≡N, that can be formed as dangling bonds at the end of graphite sheets. The average area % values of the PC0, PC1, and PC2 bands are 35, 33, and 32, respectively (Table 1).

Figure 3c corresponds to the N 1s spectrum of the $B_{0.45}C_{0.1}N_{0.45}$ NTs. The band centered at 399 eV has been deconvoluted into three bands at 397.6 (PN0), 398.6 (PN1), and 400.7 (PN2) eV, respectively. Following the assignment of the BCN films, the PN0 band can be assigned to the N−B structures. Following our previous assignment of the resolved N 1s bands of N-doped CNTs, the PN1 band can be assigned to the N atoms in the graphite-like N−C structures, and the PN2 band to the N atoms bonded to C atoms as pyridine-like structures.[19] The average area % values of the PN0, PN1, and PN2 bands are 30, 44, and 26, respectively (Table 1).

Figure 4a shows the B *1s* spectrum of the BN−C NTs measured using three photon energies (350, 475, and 912 eV). The band is asymmetrically broad in the lower energy region, which is opposite behavior to that of the pure BN NTs, but similar to that of the *h*-BN powders. This band can be deconvoluted into only two bands at 189.6 (PB0) and 190.7 (PB1) eV, corresponding to the B−C and B−N bonding structures, respectively. As the photon energy increases from 350 to 912 eV, the area % of the PB0 band decreases from 58 to 44%, due to the C outerlayers sheathing the BN NTs (Table 2). This observation is consistent with the EELS data. The width of the PB0 (B−C) band is more than twice that of the $B_{0.45}C_{0.1}N_{0.45}$ NTs. The broad electronic states of the B−C bonds suggest that the binding of the C atoms with the B atoms is

Table 1. Area % Values of the Deconvoluted Bands from the XPS B, C, and N 1s Peaks for the $B_{0.45}C_{0.1}N_{0.45}$ NTs

				photon energy					
				475 eV, (B:C:N = 0.35:0.15:0.35)		635 eV, (B:C:N = 0.35:0.15:0.35)		1265 eV, (B:C:N = 0.35:0.15:0.35)	
	band	bonding structures	position (eV)	width (eV)	area %	width (eV)	area %	width (eV)	area %
B	PB0	B−C	189.6	1.4	**36**	1.4	**34**	1.4	**38**
	PB1	B−N	190.7	1.7	**42**	2.0	**39**	2.0	**44**
	PB2	B−O	192.5	1.8	**22**	1.8	**27**	2.4	**18**
C	PC0	C−B	283.5	1.5	**34**	1.6	**37**	1.7	**34**
	PC2	C−C	284.6	1.9	**33**	2.2	**34**	2.0	**33**
	PC3	C−N	286.3	2.2	**33**	3.4	**29**	2.8	**33**
N	PN0	N−B	397.6	1.4	**28**	1.4	**31**	1.7	**30**
	PN1	graphite-like N−C	398.6	2.1	**45**	2.1	**45**	2.2	**42**
	PN2	pyridine-like N−C	400.7	1.8	**27**	1.8	**24**	1.9	**28**

Table 2. Area % Values of the Deconvoluted Bands from the XPS B, C, and N 1s Peaks for the BN−C NTs

				photon energy					
				350 eV, (B:C:N = 0.6:0.4:–)		475 eV, (B:C:N = 0.3:0.2:0.5)		912 eV, (B:C:N = 0.5:0.1:0.4)	
	band	bonding structures	position (eV)	width (eV)	area %	width (eV)	area %	width (eV)	area %
B	PB0	B−C	189.6	3.5	**58**	2.6	**54**	3.3	**44**
	PB1	B−N	190.7	1.8	**44**	1.6	**46**	2.1	**56**
C	PC0	C−B	283.4	4.2	**47**	4.2	**45**	3.2	**43**
	PC1	C−C	284.7	2.0	**53**	2.2	**55**	2.1	**57**
N	PN0	N−B	397.3			3.0	**36**	3.2	**45**
	PN1	graphite-like N−C	399.0			2.0	**64**	2.2	**55**

less effective and less homogeneous than that of the $B_{0.45}C_{0.1}N_{0.45}$ NTs. The negligible B−O bonding structures are probably due to the BN layers protected by the C outerlayers.

Figure 4b displays the C 1s spectrum, showing an asymmetric band centered at 284 eV. This can be deconvoluted into two bands at 283.4 (PC0) and 284.7 (PC1) eV, which are assigned to the C−B and C−C bonding structures, respectively. The absence of any deconvoluted band for the C−N bonding structure may be explained by the weak C−N bonds. Similarly to the B 1s result, the broadening of the PC0 (C−B) bands is significant, due to the weak bindings between the C and B/N atoms, which provides evidence for the separation of the C layers from the BN layers.

Figure 4c corresponds to the N 1s spectrum using photon energies of 475 and 912 eV. The asymmetric band centered at 399 eV has been deconvoluted into two bands at 397.3 (PN0) and 399.0 (PN1) eV, corresponding to the N−B and graphite-like N−C structures, respectively. Due to the C outerlayers, the area % of the PN1 (N−C) band is larger than that of the PN0 (N−B) band and decreases from 64 to 55% as the photon energy increases from 475 to 912 eV (Table 2). According to our previous studies of N-doped CNTs, the C atoms would be expected to bind preferentially with the N atoms via graphite-like C−N structures, when the N content is low.[19] Therefore, the absence of any deconvoluted PN3 band (pyridine-like N−C) may be related to the low N content in the C outerlayers. The broader width of the PN0 bands as compared to that of the $B_{0.45}C_{0.1}N_{0.45}$ NTs is probably caused by some inhomogenously doped C atoms in the BN layers. This interpretation of the deconvoluted bands is supported by the similar XPS spectrum of *h*-BN powders contaminated by C (Supporting Information, Figure S3 and Table S2).

3.4. XPS Valence Band Spectrum. In order to investigate the nature of the band structure, we obtained the valence band (VB) spectrum using a photon energy of 240 eV. Figure 5 displays the XPS valence band spectrum in the range 0−13 eV for the *h*-BN, $B_{45}C_{0.1}N_{0.45}$, and BN−C NTs. The spectrum of the BN NTs sample is not displayed here, due to the contribution of the CNTs in this region. The spectrum is normalized using the peak intensity at 13 eV. The zero energy is chosen at the Fermi level, E_f, which is calibrated using the threshold energy of gold foil. According to previous studies of BCN films, the emission feature between 3.5 and 11 eV is mainly due to the combinations of the C−N, C−B, and N−B 2p π-bond electrons.[7,29a] The corresponding σ-bond electrons determine the feature between 11 and 13 eV. The feature between 0 and 3.5 eV arises primarily from the *2p* electrons associated with the π bonds in the graphite structure and the N lone-pair electrons. The $B_{0.45}C_{0.1}N_{0.45}$ NTs exhibit a significant intensity in the range 3.5−13 eV, compared to the *h*-BN powders, which is probably

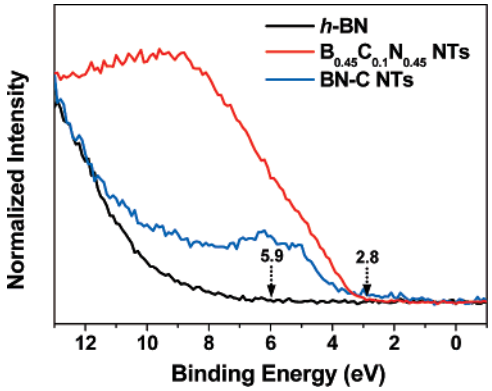

Figure 5. XPS valence band spectrum using 240 eV for the BN NTs, $B_{0.45}C_{0.1}N_{0.45}$ NTs, and BN−C NTs.

(29) (a) Ray, S. C.; Tsai, H. M.; Bao, C. W.; Chiou, J. W.; Jan, J. C.; Krishna, Kumar, K. P.; Pong, W. F.; Tsai, M.-H.; Chattopadhyay, S.; Chen, L. C.; Chien, S. C.; Lee, M. T.; Lin, S. T. Chen, K. H. *J. Appl. Phys.* **2004**, *96*, 208. (b) Ray, S.; Tsai, H.; Chiou, J.; Jan, J.; Kumar, K.; Pong, W.; Chien, F.; Tsai, M.; Chattopadhyay, S.; Chen, L.; Chien, S.; Lee, M.; Lin, S.; Chen, K. *Diamond Relat. Mater.* **2004**, *13*, 1553.

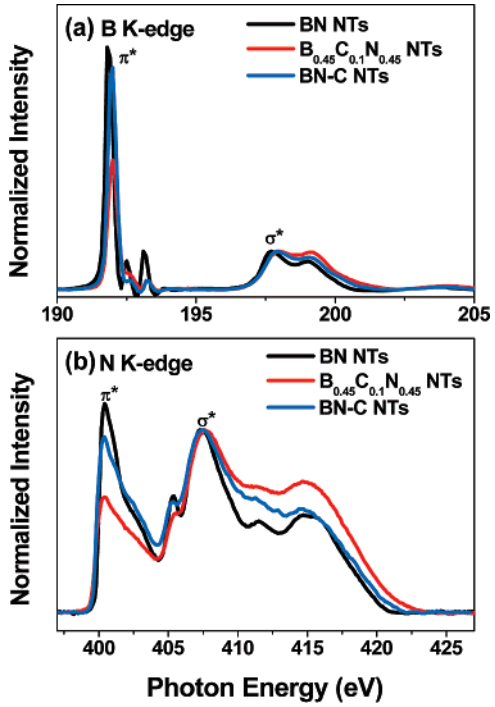

Figure 6. XANES spectra of the (a) B K-edge and (b) N K-edge of BN NTs, $B_{0.45}C_{0.1}N_{0.45}$ NTs, and BN−C NTs.

due to the increased density of states (DOS) of the pyridine-like C−N structures. In the case of the BN−C NTs, the intensity is also increased, but not as significantly as in the case of the $B_{45}C_{0.1}N_{0.45}$ NTs. It is noticed that the intensity in the 0−3.5 eV region is larger than that of the $B_{45}C_{0.1}N_{0.45}$ NTs and originates from the graphitic C outerlayers. The positions of the valence band maximum relative to the Fermi level were evaluated by taking the onset of the valence band emission and were found to be 5.9 and 2.8 eV for the *h*-BN and $B_{0.45}C_{0.1}N_{0.45}$ NTs, respectively. The DOS of the BN−C NTs in the 0−3.5 eV region causes the onset of the valence band to be lower than that of the $B_{0.45}C_{0.1}N_{0.45}$ NTs, i.e., ∼1 eV. We estimated the band gaps of the *h*-BN and $B_{0.45}C_{0.1}N_{0.45}$ NTs to be 5.9 and 2.8 eV, respectively, from their unambiguous onset.

3.5. XANES of B and N Atoms. Figure 6 shows the B and N K-edges XANES measured from the BN, $B_{0.45}C_{0.1}N_{0.45}$, and BN−C NTs. The XANES of the BN NTs was thoroughly investigated in our previous work.[30] Since the spectrum does not vary significantly with the incident angle, only the spectrum measured at an incident angle of 45° is displayed. In the B K-edge spectrum, the sharp absorption feature at 191.8 eV is due to the B 1s → π^* ($2p_z$) transition, showing a clear fingerprint of sp^2 hybridization [Figure 6a]. The broad absorption features above 197 eV can be assigned to the B 1s → σ^* ($2p_{x,y}$) transition.[29−31] A similar assignment can be made for the N K-edge spectrum, as shown in Figure 6b. The N−K edge spectrum is composed of the N 1s → π^* transition ($2p_z$) at 400.6 eV and the two major peaks corresponding to the N 1s → σ^* transitions ($2p_{x,y}$) at 408 and 415 eV, respectively.

It is important to note that the intensity ratio of the π^*/σ^* features of the $B_{0.45}C_{0.1}N_{0.45}$ NTs is much lower than that of the BN NTs. The intensity ratio of the π^*/σ^* features of the BN−C NTs is also decreased, but not as much as that of the $B_{0.45}C_{0.1}N_{0.45}$ NTs. We suggest that the incorporation of C into the *h*-BN sheets significantly decreases the π bonding states by forming defective pyridine-like C−N structures. This result is consistent with the XANES of the BCN films, in which the intensity of the π^* features in the B K- and N K-edges decreases as the C concentration increases.[31] The significant broadening of N K-edge π^* feature of the $B_{0.45}C_{0.1}N_{0.45}$ NTs as compared with that of the BN NTs could be due to the energy dispersion of the π^* band associated with the pyridine-like N structures.

3.6. Raman, CL, and PL Spectra of BN NTs, $B_{0.45}C_{0.1}N_{0.45}$ NTs, and BN−C NTs. The emission band of the $B_{0.45}C_{0.1}N_{0.45}$ NTs in the CL (at room temperature) and PL (excited by 3.815 eV at 7K) spectra is shifted to the lower energy region as compared to that of the BN NTs and BN−C NTs. This provides additional evidence for the decrease in the band gap due to the C doping (Supporting Information, Figure S4). The Raman spectrum of the $B_{0.45}C_{0.1}N_{0.45}$ NTs and BN−C NTs shows a peak at 1363 cm^{-1}, corresponding to the *h*-BN Raman active mode (Supporting Information, Figure S5). The incorporation of C atoms induces the graphite peak at 1585 cm^{-1}.

3.7. First Principles Calculation on Double-Walled BCN NT Isomers. Our calculations are based on optimized double-walled zigzag (12,0)@(20,0) BN NT conformers. Golberg et al. reported that most multiwalled BN NTs have preferentially zigzag [(*n*,0) type] chirality along their circumference, based on their electron diffraction patterns.[32] Furthermore, the BN nanotubes with radii larger than 0.6 nm are calculated to be wide band gap semiconductors with a very small dependence on the chirality.[33] Therefore, the present calculations were performed only for the zigzagged form of double-walled BCN NTs. We use LDA for the exchange-correlation functional, in order to describe the interwall interaction correctly, in view of the fact that it reproduces the interlayer interactions of graphite and *h*-BN. A (12,0)@(20,0) BN NT was built, since it shows the most favorable binding between the inner and outer shells among the (*n*,0)@(20,0) (n = 10−13) BN NTs.[34] Then, we allow various types of substitutions of the B and N atoms with the C atoms. The structure optimizations at various lattice parameters along the tube axis show that the optimal parameter of a primitive cell of an (*n*,0) BN NT containing 4*n* atoms is 4.3 Å. We use this value of the lattice parameter for all BCN NT isomers. Figure 7 displays the geometries of *Conformers I*−*III*, which we investigated herein. If not otherwise specified, the B atoms in the inner shell partly face the N atom in the outer shell, having a local AB stacking along the line L [Figure 7a]. We denote this kind of configuration as *Conformer I*. If necessary, we also investigated the other two configurations, *Conformers II and III*, in which the inner shell is displaced along the −X and +X axes with respect to the outer shell, where the N and B atoms of the inner shell are located directly beneath

(30) Choi, H. C.; Bae, S. Y.; Jang, W. S.; Park, J.; Song, H. J.; Shin, H.-J. *J. Phys. Chem. B* **2005**, *109*, 7007.

(31) (a) Gago, R.; Jiménez, I.; Albella, J. M.; Terminello, L. J. *Appl. Phys. Lett.* **2001**, *78*, 3430. (b) Gago, R.; Jiménez, I.; Sajavaara, T.; Rauhala, E.; Albella, J. M. *Diamond Relat. Mater.* **2001**, *10*, 1165. (c) Gago, R.; Jiménez, I.; Garcia, I.; Albella, J. M. *Vacuum* **2002**, *64*, 199. (d) Caretti, I.; Jiménez, I.; Gago, R.; Caceres, D.; Abendroth, B.; Albella, J. M. *Diamond Relat. Mater.* **2004**, *13*, 1532.

(32) Golberg, D.; Bando, Y.; Kurashima, K.; Sato, T. *Solid State Commun.* **2000**, *116*, 1.

(33) Rubio, A.; Corkill, J. L.; Cohen, M. L. *Phys. Rev. B* **1994**, *49*, 5081.

(34) Okada, S.; Saito, S.; Oshiyama, A. *Phys. Rev. B* **2002**, *65*, 165410.

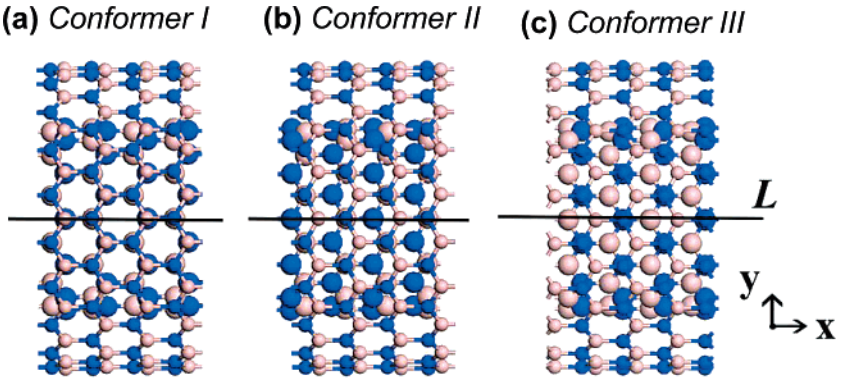

Figure 7. Three possible configurations of the inner shell with respect to the outer shell in the double-walled BCN NT: (a) *Conformer I*, (b) *Conformer II*, and (c) *Conformer III*. In *Conformers II* and *III*, the inner shell is displaced along the $-X$ and $+X$ axes with respect to the outer shell. The coordinate system is also defined.

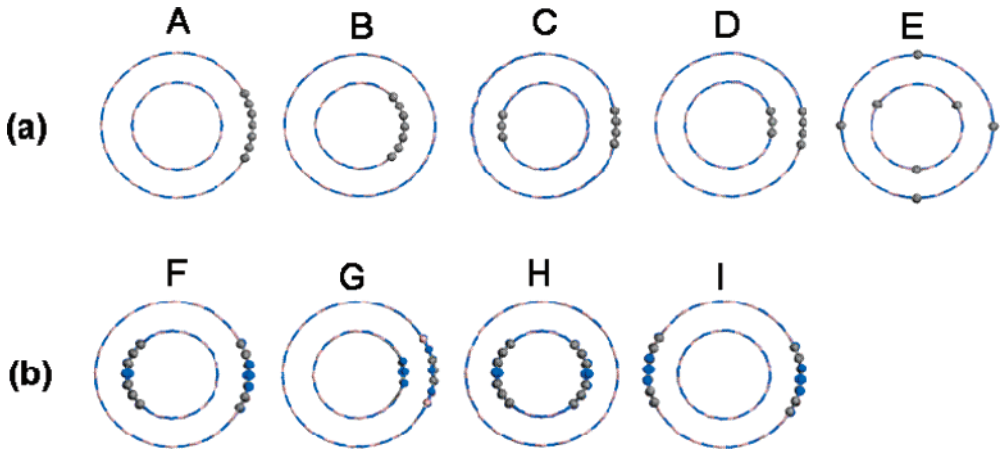

Figure 8. (a) *Isomers A*−*E* of the *s*-BCN NT, viewed along the X axis. The C atoms (black filled circles) form stripes along the tube axis. (b) *Isomers F*−*I* of the *p*-BCN NT. The atoms of the *p*-motives are indicated by filled circles: C and N atoms N_L (blue filled circles) belonging to the pyridine rings.

the center of the six-membered rings of the outer shell along the line L [Figure 7b and 7c].

Next, we investigated the (12,0)@(20,0) BCN NTs with a B/N ratio of exactly 1 and no defects (hereafter referred to as "*s*-BCN NTs"). Starting from the primitive cell of the (12,0)@(20,0) BN NT with 128 atoms, the BCN NT with ∼10% C is constructed by replacing 7 N and 7 B atoms with 14 C atoms. The BCN NT with 5% C doping is also generated by replacing 3 N and 3 B atoms with 12 C atoms. Similarly, 20% C doping is achieved by replacing 13 N and 13 B atoms with 26 C atoms. Figure 8a shows the geometries of these *isomers*, *A*−*E*. Note that these C contents are still smaller than that of the BN−C NTs, in which the C-content in the outerlayers is approximately 80% (EELS data). Our structure optimization was done using four *k*-points in the irreducible region of the first Brillouin zone along the tube axis, which guarantees the accuracy of the total energy to within 1 meV. For all of the isomers, the C atoms form a stripe along the tube axis. Figure 9a displays the structures of the 10% C-doped *Isomer A*. The formation of the striped C−C layer segregated from the B−N layer is consistent with the results of previous works on BC_2N sheets.[5]

Table 3 lists the relative energies of the five *isomers*, *A*−*E*. The most stable isomer, *Isomer A*, is characterized by C substitutions exclusively on the outer shell. On the other hand, *Isomer B* has C atoms exclusively in the inner shell, also forming a stripe along the tube. In the case of 5% substitution, *Isomers C*−*D* have two and six C atoms in the inner and outer shells, respectively. This represents approximately the same C content, 5%, in the inner and outer shells. In the case of 10% substitution, these two isomers have four and eight C atoms in the inner and outer shells, respectively. *Isomer A* is the most stable. *Isomer B* is the second most stable, and the stability decreases as the C content increases. In the case of a C content of 5% and 20%, the energy differences between the two *Isomers A* and *B* are 0.08 and 0.51 eV, respectively. This indicates that the C atoms tend to locate more preferentially on the outer shell as the C content increases.

Next, we investigate the (12,0)@(20,0) BCN NT isomers with pyridine-like local structures (hereafter referred to as "*p*-BCN NTs"), in order to simulate the structure of the $B_{0.45}C_{0.1}N_{0.45}$ NTs. The local structures of the *p*-BCN NTs are similar to the hollow structure of the N-doped CNTs identified experimentally by Czerw et al.[35] In order to generate such a hollow structure in a BN NT, we take a supercell with two primitive cells of (12,0)@(20,0) BN NT as the starting material. It consists of 96 and 160 atoms in the inner and outer shells of the tube, respectively. Half of these atoms are N atoms, and the other half are B atoms. From the BN NT, we build a motif, referred

(35) Czerw, R.; Terrones, M.; Charlier, J.-C.; Blasé, X.; Foley, B.; Kamalakaran, R.; Grobert, N.; Terrones, H.; Tekleab, D.; Ajayan, P. M.; Blau, W.; Ruhle, M.; Carroll, D. L. *Nano Lett.* **2001**, *1*, 457.

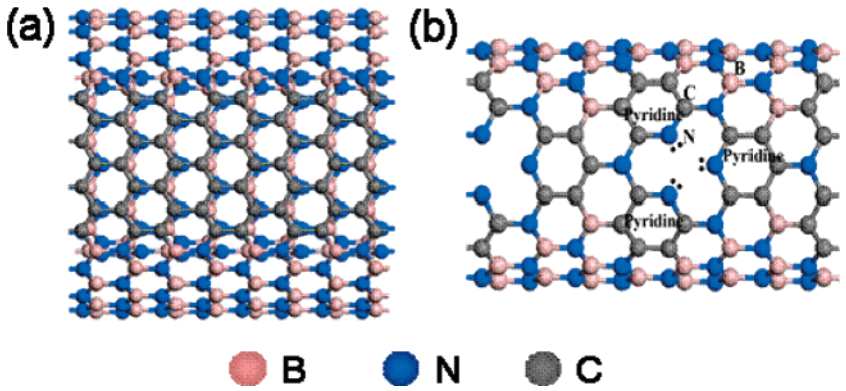

Figure 9. (a) *Isomer A* of the *s*-BCN NT projected onto the *XY* plane. The C atoms form a stripe along the *X* axis. For a better understanding, two primitive cells are shown. The pink, blue, and black colored filled circles represent the B, N, and C atoms, respectively. (b) A local *p*-motif with three pyridine rings in the inner shell of *p*-BCN NTs. Note that the underlying primitive cell is twice as large as that for the *s*-BCN NTs.

Table 3. Relative Energies (in eV) of the Five Isomers of the Double-Walled *s*-BCN NT Containing 5, 10, and 20% C Atoms

	isomer				
C-content	A	B	C	D	E
5%	0	0.08	1.86	1.80	
10%	0	0.25	1.97	2.02	11.16
20%	0	0.51			

to as "*p*-motif", as shown in Figure 9b, according to the following procedure: (1) we delete a B atom (=B_d) to produce a hole, (2) we change each of the three six-member rings to a pyridine ring by substituting two N atoms and three B atoms by five C atoms, the rings originally being bonded to the atom, B_d, before being deleted. A supercell of a *p*-BCN NT is assumed to have two such *p*-motives.

Figure 8b displays the geometries of the $B_{0.43}C_{0.12}N_{0.45}$ NTs (four *isomers*, *F*−*I*), consisting of 108 B atoms, 30 C atoms, and 116 N atoms, in the supercell, whose B/C/N ratio is very close to that of the $B_{0.45}C_{0.1}N_{0.45}$ NTs. Although there are a number of possible isomers in a *p*-BCN NT with two *p*-motives, we consider 12 typical isomers. *Isomers F and G* are defined as having one motif on the inner shell and the other one on the outer shell. In *Isomer G*, the two *p*-motives directly face each other, while they are far from each other in *Isomer F*. *Isomers H and I* have exclusively two motives in the inner and outer shells, respectively. Each isomer is further divided into three, *Conformers I*−*III*, depending upon the relative displacement of the outer shell with respect to the inner shell. The relative energies of the 12 isomers are listed in Table 4.

Our structure optimizations using *k*-point sampling with two *k*-points in the irreducible region of the first Brillouin zone show that the energy levels of all 12 isomers are within 0.29 eV of each other. The most stable isomer is *Isomer H-II*, followed by *Isomer H-III*, in which the *p*-motives are located exclusively on the inner shell. The next stable isomer, *Isomer F-III*, in which the motives are distributed in both shells, is marginally (=0.04 eV) less stable than *Isomer H-II*. *Isomers I-I*−*I-III*, in which the motives are exclusively located on the outer shell are the least stable, which clearly contrasts with the characteristics of the *s*-BCN NTs for which the corresponding isomer is the most stable. The very small energy difference between *Isomers H-II and F-III* indicates that the relative population of the corresponding isomers in the case of the multiwalled BCN NTs will be mainly determined by the "entropic" factor. Namely, "BN-outerlayered CNT", which corresponds to *Isomers H-II* and *H-III*, would be expected to be "entropically" quite unfavorable. Remarkably, however, there are a vast number of possible configurations in which the *p*-motives are equally distributed over all of the shells. In short, the *p*-BCN NT will be dominated by the isomer in which the *p*-motives are distributed over all of the shells, which is consistent with the experimental result obtained for the $B_{0.45}C_{0.1}N_{0.45}$ NTs.

In order to assess the stability of the *p*-motif, we compared its energy with that of another motif, referred to as "*q*-motif", as shown in the Supporting Information, Figure S6. It consists of three contiguous carbon rings substitutionally embedded in a BN NT, with the central pyridine ring originally bonded to B_d. It has exactly the same numbers of B and N atoms substituted by C atoms as a *p*-motif. Two other rings, originally bonded to B_d, are connected by an N−N bond.[22f,36] Our calculation on the local stabilities of the two motives indicated that the *p*-motive is substantially more stable than the *q*-motives, by 1.23 eV. We concluded the *p*-motif will presumably represent the best pyridine-like local structure of the BCN NTs.

The electronic density of states (DOS) for the 10% C-doped *Isomer A* (*s*-BCN NT) is displayed in Figure 10a, along with that of a pure (12,0)@(20,0) BN NT. We observe a large shift (=1.5 eV) of the Fermi level toward a higher energy upon the C substitution. Many new carbon states are introduced inside the range [−2,2] eV around the Fermi level, indicating that the electric conduction will occur mainly through the carbon stripe in the *s*-BCN NT. The peak which appeared at ∼2.0 eV corresponds to the carbon states which form stripes of electron density along the tube axis. Apart from this peak, the DOS curve is almost symmetrical about the Fermi level, as in the case of the pure BN NT.

The electronic DOS for *Isomer F*−*III* (*p*-BCN NT) is displayed in Figure 10b, along with that of the (12,0)@(20,0) BN NT. In contrast to the cases of the pure BN NT and *s*-BCN NT, the curve is highly asymmetrical about the Fermi level. New states are introduced in the region [−2.0, 2.5] eV, significantly reducing the band gap from 3.82 to 1.68 eV. Our separate analysis of the band structure shows that this material is still a semiconductor with a direct gap at the Γ-point, rendering it useful for optoelectronic devices. This result is different from the studies of Czerw et al., in which the N-doping

(36) Schmidt, T. M.; Baierle, R. J.; Piquini, P.; Fazzio, A. *Phys. Rev. B* **2003**, *67*, 113407.

Table 4. Relative Energies (in eV) of the Twelve Isomers (*Conformers I−III* of *Isomers F−I*) of the Double-Walled *p*-BCN NTs

	F-I	*F-II*	*F-III*	*G-I*	*G-II*	*G-II*	*H-I*	*H-II*	*H-III*	*I-I*	*I-II*	*I-III*
E (eV)	0.14	0.07	0.04	0.18	0.19	0.18	0.08	0	0.01	0.29	0.34	1.33

in the CNTs converts semiconducting tubes to metallic ones.[35] Apparently, the calculated band gap (=1.68 eV) is smaller than that (=2.8 eV) of the multiwalled $B_{0.45}C_{0.1}N_{0.45}$ NTs obtained from our XPS spectra. However, we want to point out that the LDA usually underestimates the band gap.[4b] In this regard, we recall that the LDA band gap (~4 eV) of single-walled BN NTs (radii >0.6 nm) is also smaller than our experimental value (=5.9 eV).[33] Therefore, we believe that the double-walled *p*-BCN NT is a reasonable model for the multiwalled $B_{0.45}C_{0.1}N_{0.45}$ NTs.

The spatially localized lone-pair states of the nitrogen atoms (=N_L) of the pyridine-like local structure are located below the Fermi level in the interval [−2.0,−0.4] eV. The HOMO band is one of these states. Due to the large distance between the inner and outer shells of the double-walled tube, there is no appreciable interaction between the lone-pair states of the two shells. The comparison of the DOS for the *s*- and *p*-BCN NTs in the range [−2.0, 0.0] eV shows that the lone-pair states of the *p*-BCN NT produce a much higher DOS than the carbon states (=C bands) of the *s*-BCN NT. The electron density of the C-bands of the *p*-BCN NT located in the range [−2.0, 2.0] eV is delocalized over the C−N_L region. It forms a stripe along the tube axis, similarly to the case of the C-bands of the *s*-BCN NTs. The LUMO and LUMO + 1 bands are two such C-bands, whose electron densities are exclusively concentrated on the inner and outer shells, respectively. Figure 10c displays the stripe formation of the electron density in the LUMO + 1 band. Although it is not shown here, this feature is manifested in the dispersions of the C-bands in the band structure. [Note that all of the bands of the (12,0)@(20,0) BN NT are almost flat in the energy range that we are concerned with.] This kind of delocalization would increase the stability of the *p*-BCN NTs significantly. In addition, the *p*-BCN NT exhibits a much more pronounced DOS peak than the BN NT at ~2.0 eV, which is similar to the case of the *s*-BCN NT. Our separate analysis shows that this peak can be ascribed to the states in which the electron density forms a stripe along the tube axis at the boundary of the BN (=region other than C−N_L region) and C−N_L regions. In short, the peak at ~2.0 eV originates from the formation of a striped carbon region (including the atom N_L) along the tube axis.

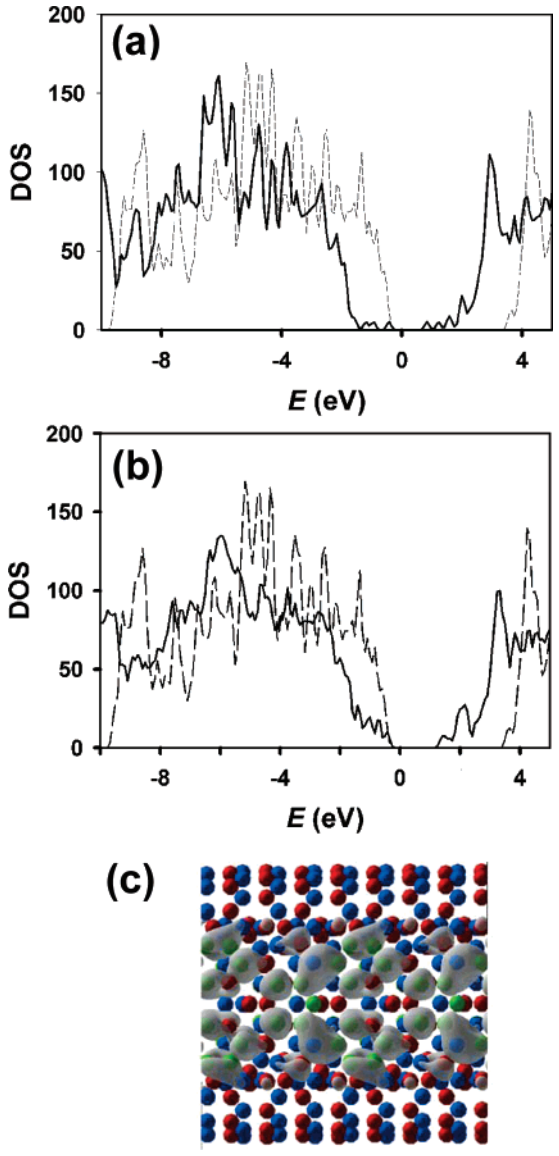

Figure 10. (a) Electronic DOS for the (12,0)@(20,0) BN NT (dashed) and *Isomer A* of the *s*-BCN NT (solid). (b) Electronic DOS for the (12,0)@-(20,0) BN NT (dashed) and *Isomer F-III* of the *p*-BCN NT (solid). The Fermi level is separately set to zero for each of them. (c) Electronic density distribution in the LUMO + 1 band of the *p*-BCN NT (*Isomer F-III*). For clarity, the inner shell is not shown.

4. Discussion

The two types of multiwalled BCN NTs, $B_{0.45}C_{0.1}N_{0.45}$ NTs, and BN−C NTs, were categorized on the basis of their distinctive structures. The EELS of the individual nanotubes and XPS data confirm that the C atoms of the $B_{0.45}C_{0.1}N_{0.45}$ NTs are homogenously distributed over the entirety of the nanotubes, whereas those of the BN−C NTs are separated from the BN NTs in the form of outerlayers. From the state-resolved B, C, and N 1s and valence band spectra of XPS, and the XANES, we found that the $B_{0.45}C_{0.1}N_{0.45}$ NTs have the following properties: (1) there exists significant bonding structures of B−C and C−N; (2) the pyridine-like C−N bonding structures are formed; (3) the band gap is estimated to be 2.8 eV; (4) the C doping significantly decreases the π bonding structures of the BN layers, due to the defective pyridine-like bonding structure. On the other hand, the BN−C NTs have the following properties: (1) the C outerlayers protect against the surface oxidization of the BN NTs; (2) there is negligible bonding between the C and B/N atoms, so the π bonding states of the BN layers are slightly reduced; (3) graphite-like C−N structures are possibly formed in the C outerlayers.

Despite the existence of a number of works on the synthesis of BCN NTs with a homogeneous BCN composition and also with separated phases of BN and C layers,[11−18] no controlled formation of these distinctive BCN NTs has yet been reported.

Moreover, their electronic states have not been discussed in detail. Herein, we controlled the synthesis of BCN NTs with a homogeneous and separated composition of C atoms, by adjusting the growth condition of CVD; the BN−C NTs are preferentially produced at a lower C concentration, and the $B_{0.45}C_{0.10}N_{0.45}$ NTs, at a higher C concentration. The use of a high-resolution X-ray source enabled us to resolve the B, C, and N 1s spectra with high reliability, thus allowing us to clearly identify the different types of electronic structures of the B, C, and N atoms involved in the homogeneous and segregated C atom distribution in the BCN NTs.

First principles calculations were carried for the double-walled BCN NTs, providing a systematic tool for the interpretation of the experimental results. Of course, we did not make any calculations for the multiwalled tubes, since this is practically impossible due to the very large number of atoms involved. We demonstrated that the calculation results obtained for the double-walled (12,0)@(20,0) BCN NTs can be extrapolated to the multiwalled tubes. The calculation suggests that the condition which produces exclusively the BN−C NTs is as follows; (1) a constant B/N ratio of 1 and (2) no pyridine-like structures or defects. In fact, *Isomer A* of the *s*-BCN NT corresponds to two shells of the BN−C NTs at the boundary of the inner BN NTs and outer CNTs and is more favorable "entropically" than the *Isomer B* (C atoms only in the inner shell), since there are many more ways of achieving the same configuration, due to the larger size of the outer shell. In addition, the *Isomers C*−*E*, whose C atoms are distributed in both the inner and outer shells of the tube, are at least 1.86 eV less stable than *Isomer A* and, thus, can be safely excluded from the list of possible products. The relative stabilities of the various isomers also show that the substituted C atoms tend to locate on the outer shell of the tube by forming a continuous stripe. Thus, the C-outerlayered BN tubes would be expected to be energetically the most stable, as well as entropically favorable, when only graphite-like structures are allowed.

Based on the XPS data of $B_{0.45}C_{0.10}N_{0.45}$ NTs showing the existence of pyridine-like C−N structures, it is quite reasonable to conjecture that the pyridine-like local structure is accompanied by the formation of hollow sites in the form of *p*-motives. This conjecture was strongly supported by the stability of the motif which is much more pronounced than that of another possible candidate (*q*-motif). Interestingly, our calculations on the *p*-BCN NTs with the local pyridine-like structures reveal that the C atoms tend to distribute homogeneously over all of the shells of the double-walled BCN NTs. This dispersed distribution of the C atoms is predominantly driven by entropy. It is quite evident that this tendency will be much more pronounced in the multiwalled tubes. Whether or not such a distribution is also driven by energy for the case of the multiwalled tubes is outside the scope of this work, because large numbers of atoms must be involved in such a calculation. However, our calculation, at least, suggests the possibility that the homogeneous distribution of the C atoms is one of the most energetically favorable distributions in the multiwalled $B_{0.45}C_{0.10}N_{0.45}$ NTs.

The valence band XPS spectrum suggests that the band gaps of the *h*-BN powders and $B_{0.45}C_{0.1}N_{0.45}$ NTs are 5.9 and 2.8 eV, respectively. The band gap of 5.9 eV for the *h*-BN powders is consistent with the band gap energy of BN film (about 6 eV). The band gap of the $B_{0.45}C_{0.1}N_{0.45}$ NTs would be expected to be 2.8 eV, which is about 3 eV lower than that of the bulk *h*-BN. The band gap of $B_{0.45}C_{0.1}N_{0.45}$ is predicted to be higher than that of the BC_2N (1.4, 1.6, or 2.1 eV) film, due to the lower C content.[7] Thus, the present value is quite reasonable, taking into account the lower C content. The calculation of the DOS indicates the introduction of new states in the [−2.0, 2.5] eV region, reducing significantly the band gap from 3.82 eV (BN NTs) to 1.68 eV. This estimated band gap is smaller than that (=2.8 eV) of the multiwalled $B_{0.45}C_{0.1}N_{0.45}$ NTs. As already mentioned (in the Results section 3.7), the LDA usually underestimates the band gap, and thus, we believe that it predicts correctly the decrease in the band gap due to the C doping. Although the carbon defects (pyridine-like local structure, i.e., *p*-motif) affect the electronic structure of the tube, the BCN NTs still preserve the semiconducting nature.

5. Conclusions

The multiwalled $B_{0.45}C_{0.1}N_{0.45}$ NTs (10% C doped BN NTs) and BN−C NTs (C outerlayered BN NTs) were synthesized via the thermal CVD of B/BN/FePc under NH_3 flow at 1200 °C. They both have a bamboolike structure with an average diameter of about 100 nm. The EELS and XPS data reveal the homogenously doped 10% C contents for the $B_{0.45}C_{0.1}N_{0.45}$ NTs and 5-nm-thick C outerlayers for the BN−C NTs. The band deconvolution of XPS reveals significant binding states of B−C and C−N, as well as the existence of a pyridine-like C−N structure. The 10% C doping decreases drastically the π bonding states of the B and N atoms. From the XPS valence band spectrum, the band gap was estimated to be 2.8 eV. In contrast, the state-resolved XPS of the BN−C NTs suggests that there is negligible binding between the C and B/N atoms, indicating the segregation of the C layers from the BN nanotubes. The binding of C−N in the C layers occurs mainly through the graphite-like structures.

Using the first principles method based on DFT theory, we calculated the total energy of various possible isomers of the double-walled (12,0)@(20,0) C-doped BN NTs. When there exist no defects in the tubes with B/N = 1.0 and the graphite-like structures (*s*-BCN NTs), the most stable isomers are formed by the segregation of the C atom layers preferentially at the outer wall. This structure represents a reasonable structural model for the BN−C NTs. When there are local pyridine-like structures with hollow defects (*p*-BCN NTs), the C atoms distribute homogeneously over the two shells in the form of *p*-motives, corresponding to the structure of the $B_{0.45}C_{0.1}N_{0.45}$ NTs. The characteristics of the electronic DOS were identified, and the decrease in the band gap due to the C doping was found to be consistent with the experimental results. Finally, we suggest that the present experimental and theoretical studies of BCN NTs will lead to a better understanding of the electronic structure of BCN nanostructures, which is prerequisite to their application as nanoelectronic devices.

Acknowledgment. This work was supported by KRF grants (R14-2003-033-01003-0; R02-2004-000-10025-0; 2003-015 C00265). The SEM and HVEM measurements were performed at the Korea Basic Science Institute. The experiments at the PLS were partially supported by MOST and POSTECH. The theoretical part of this work was supported by a Korea Research Foundation Grant funded by the Korean Government (MOEHRD) (KRF-2005-041-C00211).

Supporting Information Available: Survey-scanned XPS of the BN NTs, $B_{0.45}C_{0.1}N_{0.45}$ NTs, and BN−C NTs; fine-scanned B and N 1s XPS of the BN NTs and *h*-BN powders; CL, PL, and Raman spectra of the BN, $B_{0.45}C_{0.1}N_{0.45}$, and BN−C NTs; the structure of a *q*-motif. This material is available free of charge via the Internet at http://pubs.acs.org.

JA067592R